Engineering Analysis with Boundary Elements 36 (2012) 404–415

Contents lists available at SciVerse ScienceDirect

Engineering Analysis with Boundary Elements

journal homepage: www.elsevier.com/locate/enganabound

A precorrected-FFT higher-order boundary element method for wave–body problems

Sheng-chao Jiang [a], Bin Teng [a,*], Ying Gou [a], De-zhi Ning [a,b]

[a] State Key Laboratory of Coastal and Offshore Engineering, Dalian University of Technology, Dalian 116024, China
[b] Key Laboratory of Renewable Energy and Gas Hydrate, Chinese Academy of Sciences, Guangzhou 510640, China

ARTICLE INFO

Article history:
Received 10 December 2010
Accepted 2 August 2011
Available online 26 October 2011

Keywords:
HOBEM
pFFT
Infinite water depth
Free-surface Green function
Computational time
Computer memory

ABSTRACT

The boundary element method (BEM) has been widely applied in the field of wave interaction with offshore structures, but it is still not easy to use in resolving large-scale problems because of computing costs and computer storage being increased by $O(N^2)$ for the traditional BEM. In this paper a precorrected Fast Fourier Transform (pFFT) higher-order boundary element method (HOBEM) is proposed for reducing the computational time and computer memory by $O(N)$. By using a free-surface Green function for infinite water-depth, the disadvantage of the Fast Multipole Boundary Element Method (FMBEM)—i.e. unable to solve infinite deep-water wave problems—can be overcome. Numerical results from the problems of wave interaction with single- and multi-bodies show that the present method evidently has more advantages in saving memory and computing time, especially for large-scale problems, than the traditional HOBEM. In addition, the optimal variable of pFFT mesh is recommended to minimize time cost.

Crown Copyright © 2011 Published by Elsevier Ltd. All rights reserved.

1. Introduction

In analyzing hydrodynamic interaction problems between body and free surface waves, the boundary element method (BEM) is currently more popular than volume methods such as the finite element method (FEM), finite volume method (FVM), etc., because of the dimensions reduced by one and a smaller number of unknowns obtained. Once the free-surface Green function is applied, the unknowns need only to be distributed on the body surface. The computation cost and the workload to be prepared before calculation can be reduced. Based on these advantages, the constant panel method (CPM) introduced by Hess and Smith [1] has been widely used [2,3]. In this method, the submerged body surface alone is discretized by a set of quadrilateral or triangular flat panels. Pulsating sources or sinks are placed at the centers of all panels, the strengths of these sources being constant in each panel. For a body with a curved surface, however, such a representation allows 'leaks' between panels, with the result that large numbers of panels are required to achieve sufficiently accurate results. Therefore, the use of HOBEM for such problems has been investigated by Liu et al. [4], Eatock Taylor and Chau [5], Eatock Taylor and Teng [6], Teng and Eatock Taylor [7]. In the HOBEM, the body surface can be discretized by curvilinear triangular or rectangular elements. Each element is described by fitting the nodes by an expansion using interpolating polynomials as their shape functions. There are no 'leaks' at the common boundary of the neighboring elements and the velocity potentials are continuous on the whole body surface. This method could give more accurate results than CPM for the same computational effort, together with minimum computer storage and CPU time.

Unfortunately, traditional BEMs are computationally expensive, because of a dense linear system of equations generated. The computational cost (time expended and memory allocated) of solving such a dense system is, at least, $O(N^2)$, where N is the number of unknowns. It limits the use of the BEM only to medium-size problems, even if the HOBEM is employed [8]. However, with the development of ocean engineering, large-scale ships (such as FPSO), deepwater platforms, floating boatyards, mobile offshore bases (MOB) and multiple floating bodies, etc., are given more attention [9,10]. The advantage of the BEM is removed by the drawback for large-scale problems, so that the computational cost of the BEM is larger than that of a robust multi-grid technology applied to a domain-type method, such as finite difference or finite element [11]. Therefore, the accelerated technique must be implemented in the BEM.

Various methods have been developed to reduce the computational time and memory for the traditional BEM, such as the Fast Multipole Method (FMM) and the precorrected Fast Fourier

* Corresponding author.
E-mail addresses: jiangshengchao@foxmail.com (S.-c. Jiang), bteng@dlut.edu.cn (B. Teng).

0955-7997/$ - see front matter Crown Copyright © 2011 Published by Elsevier Ltd. All rights reserved.
doi:10.1016/j.enganabound.2011.08.002

Transform (pFFT) method. The central idea of these methods is to systematically approximate the influence of the kernel between source- and field-points, which are sufficiently far apart relative to the element size, and to reduce the time for the matrix–vector operation in the iterative method of the solution. The FMM is based on the use of multipole expansion to the free surface Green function. The influence of the Green function is calculated by systematic application of Graf's addition theorem of the Bessel and Hankel functions following the hierarchical algorithm [12]. Utsunomiya and Watanabe [13,14], Teng and Gou [15] applied this technique in the HOBEM for floating boatyard problems. However, the FMM is expected to be less efficient for deep water owing to slow convergence of multipole expansion of the free-surface Green function [16]. Compared with the FMM, the pFFT method can be proposed for the integral equations with a general form of Green function and solve the wave–body problem in infinite water-depth. In this method, the input geometry is overlaid with a rectangular grid, and the influence of the singularity distribution on the body elements is represented by the influence from grid singularities lying on the grid. This uniform grid representation allows the FFT to be used for the efficient evaluation and for the product with the solution vector in the iterative solution method. The computational time for the evaluation and its product with the solution vector is $O(N_g \log N_g)$ effort, where N_g is the number of nodes on the grid. This method was employed in integral equation method by Phillips and White [17] for electro-static and electro-dynamic applications, and subsequently was extended to the analysis of wave–body interactions by Korsmeyer et al. [18]. Kring et al. [19] applied this method to large, complex offshore structures. However, the above works are all based on the constant panel method. In this paper, a precorrected Fast Fourier Transform higher-order boundary element method (pFFT-HOBEM) is developed to reduce the computational time and computer memory. Compared with the previous method, the present method can be used with substantial reductions of computer time to achieve the same or higher accuracy. In addition, the accuracy and continuity of the solution could be improved. This is particularly important for structural analysis, as accurate values of the local hydrodynamic pressure can be transferred to finite element programs [20].

In Section 2, the mathematical description of the higher-order boundary method for wave radiation–diffraction problem is introduced. The basic theory and numerical procedure of the pFFT-HOBEM is described in Section 3. In Section 4, the proposed method is validated, and the efficiency is demonstrated through examinations of the computation time and memory for isolated bodies and multi-bodies.

2. Boundary integral equations

A Cartesian coordinate system $\mathbf{x}=(x, y, z)$ is defined with $z=0$ for the plane of the undisturbed free surface. It is assumed that the fluid is incompressible and inviscid, and the flow is irrotational. The fluid velocity is then represented by the gradient of the velocity potential $\Phi(\mathbf{x},t)$ satisfying the Laplace equation in the fluid domain:

$$\nabla^2 \Phi = 0 \tag{1}$$

As shown in Fig. 1, the fluid depth is infinite. The portion of the body below the plane $z=0$ is referred to as the submerged surface S_B. This surface is assumed to be impermeable, with its normal velocity equal to the normal component of the fluid velocity. At far-field from the structure, the waves are composed of a prescribed incident waves and outgoing waves associated with diffraction and radiation.

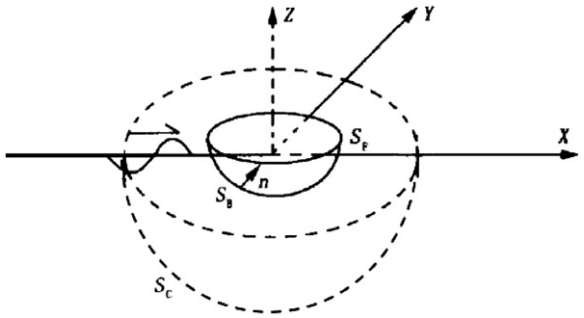

Fig. 1. Definitions of computational domain and boundaries.

Under the assumption of small, unsteady motions relative to the wavelength, the free surface boundary condition can be linearized about its mean position. The body boundary condition can also be linearized about its mean position if the structure is not fixed. Owing to the time-harmonic dependence, the use of a complex notation for all oscillatory quantities is applied. Thus the velocity potential is expressed as:

$$\Phi = \mathrm{Re}[\phi e^{-i\omega t}] \tag{2}$$

where ω is the incident regular wave angular frequency or angular frequency of body motion. The complex spatial potential ϕ must satisfy the following linearized free surface S_F, body surface S_B and infinite seabed boundary conditions besides the Laplace equation:

$$\frac{\partial \phi}{\partial z} = \frac{\omega^2}{g}\phi, \text{ on } S_F \tag{3}$$

$$\frac{\partial \phi}{\partial n} = v_n, \text{ on } S_B \tag{4}$$

$$\phi = 0, \ z = -\infty \tag{5}$$

where g is the acceleration owing to the gravity, n and $\vec{v_n}$ are the unit normal vector and the normal velocity of points on the body surface, respectively. Generally, n points out of the fluid domain and thus towards the inside of the body.

The linearization permits the decomposition of the velocity potential in the alternative forms:

$$\phi = \phi_i + \phi_d + \phi_r \tag{6}$$

where ϕ_i is the potential of the incident wave, defined by:

$$\phi_i = -\frac{igA}{\omega} e^{kz} e^{ik(x\cos\beta + y\sin\beta)} \tag{7}$$

where A is the wave amplitude, and β is the incident wave angle. The wave number k is the positive real root of the dispersion relation $\omega^2 = gk$. Except for the incident wave potential ϕ_i, all the other wave components are needed to satisfy the radiation condition of outgoing waves in the far field, i.e., the Sommerfeld condition.

In Eq. (6), the diffraction potential ϕ_d and the radiation potential ϕ_r owing to the presence of the body, are subject to their boundary conditions as follows:

$$\frac{\partial \phi_d}{\partial n} = -\frac{\partial \phi_i}{\partial n}, \text{ on } S_B \tag{8}$$

$$\frac{\partial \phi_r}{\partial n} = \vec{v_n}, \text{ on } S_B \tag{9}$$

The radiation potential ϕ_r represents the fluid disturbance due to the motions of the body and can be expressed in the form:

$$\phi_r = \sum_{j=1}^{6} -i\omega\xi_j\phi_j \tag{10}$$

where (ξ_1, ξ_2, ξ_3) are the amplitudes of body translation and $(\xi_4, \xi_5, \xi_6) = (\alpha_x, \alpha_y, \alpha_z)$ the amplitudes of body rotation. We define ϕ_j as the radiation potential corresponding to a unit body velocity in the jth body freedom. By substituting Eq. (10) into (9), the boundary condition of the body surface is then expressed in the following form:

$$\frac{\partial \phi_j}{\partial n} = n_j, \text{ on } S_B \tag{11}$$

where (n_1, n_2, n_3) is the unit normal vector of the body surface, $(n_4, n_5, n_6) = (\mathbf{x}-\mathbf{x}_0) \times \mathbf{n}$, and $\mathbf{x}_0$ is the coordinates of the rotation center. Similarly, note $\phi_0 = \phi_i$ and $\phi_7 = \phi_d$, the body conditions of diffraction and radiation potential, which can be written together as follows:

$$\frac{\partial \phi_j}{\partial n} = \begin{cases} n_j, & (j = 1,\ldots,6) \\ -\frac{\partial \phi_0}{\partial n}, & (j = 7) \end{cases} \tag{12}$$

The infinite depth free surface Green function $G(x,x_0)$ is used as follows [21]:

$$G = G_T + G_H = \frac{1}{r} + \int_0^\infty \frac{\lambda + k}{\lambda - k} e^{\lambda(z+\zeta)} J_0(\lambda R) d\lambda \tag{13}$$

where $r = [R^2 + (z-z_0)^2]^{1/2}$, and R is the horizontal distance between field and source points. In the development of the Green function computation, Noblesse's [22] and Newman's [23] important works on the approximation of free-surface Green functions have been instructive.

Applying the second Green's theorem to potential ϕ and the Green function $G(x,x_0)$, we can obtain the boundary integral equation as follows:

$$\alpha \phi_j(x_0) - \iint_{S_B} \frac{\partial G(x,x_0)}{\partial n} \phi_j(x) dS = \begin{cases} -\iint_{S_B} n_j G(x,x_0) dS, & (j = 1,\ldots,6) \\ \iint_{S_B} G(x,x_0) \frac{\partial \phi_0(x)}{\partial n} dS, & (j = 7) \end{cases} \tag{14}$$

where the free-term α is the solid-angle coefficients. Its value changes with the position of the source point x_0 and could be evaluated according to the geometric character [24].

A set of linear equations are obtained after the integral Eq. (14) discretized. Diffraction and radiation potentials on the body surface can be resolved from the set of linear equations. Then the exciting forces and hydrodynamic coefficients are obtained by Bernoulli's equation and integration of wave pressure over the body surface. The exciting forces can be written into

$$F = \mathrm{Re}[f e^{-i\omega t}] \tag{15}$$

where

$$f = i\omega\rho \iint_{S_B} (\phi_0 + \phi_7) \cdot \vec{n}\, dS \tag{16}$$

and the hydrodynamic coefficients can be expressed as

$$\omega^2 a_{ji} + i\omega b_{ji} = \omega^2 \rho \iint_{S_B} \phi_j n_i dS, \quad (i,j = 1,\ldots,6) \tag{17}$$

where a_{ji} and b_{ji} are added mass and radiation damping, respectively.

For field points in the fluid, it is straightforward to evaluate the potential as given by (14) with the solid-angle coefficients being 1. The appropriate representations in this case are

$$\phi_j(x_0) = \iint_{S_B} \frac{\partial G(x,x_0)}{\partial n} \phi_j(x) dS + \begin{cases} -\iint_{S_B} n_j G(x,x_0) dS, & (j = 1,\ldots,6) \\ \iint_{S_B} G(x,x_0) \frac{\partial \phi_0(x)}{\partial n} dS, & (j = 7) \end{cases} \tag{18}$$

And then, the wave elevation can be written as

$$\zeta = \mathrm{Re}[\eta(x,y) e^{-i\omega t}] \tag{19}$$

where

$$\eta(x,y) = \frac{i\omega}{g} \sum_{j=0}^{7} \phi_j \tag{20}$$

3. Precorrected fast Fourier transform method

In the higher-order boundary element method, the body surface can be discretized by N_E isoparametric elements. After introduction of shape functions $h^k(\xi,\eta)$ in each element, the velocity potential and its derivatives within an element can be written in terms of nodal values in the following form:

$$\begin{aligned} \phi(\xi,\eta) &= \sum_{k=1}^{K_e} h^k(\xi,\eta) \phi^k \\ \frac{\partial \phi(\xi,\eta)}{\partial \xi} &= \sum_{k=1}^{K_e} \frac{\partial h^k(\xi,\eta)}{\partial \xi} \phi^k \\ \frac{\partial \phi(\xi,\eta)}{\partial \eta} &= \sum_{k=1}^{K_e} \frac{\partial h^k(\xi,\eta)}{\partial \eta} \phi^k \end{aligned} \tag{21}$$

where K_e is the number of nodes (6 for triangle, 8 for quadrilateral) in the element, ϕ^k are the nodal potentials and (ξ,η) are local intrinsic coordinates. By substituting this representation into Eq. (14), the integral equation can be written in such a discretized form as

$$\begin{aligned} &\alpha \phi_j(x_0) - \sum_{e=1}^{N_E} \int_{-1}^{1} \int_{-1}^{1} h^k \phi_j^k(x) \frac{\partial G(x,x_0)}{\partial n} |J_e(\xi,\eta)| d\xi d\eta \\ &= \begin{cases} -\sum_{e=1}^{N_E} \int_{-1}^{1} \int_{-1}^{1} n_j G(x,x_0) |J_e(\xi,\eta)| d\xi d\eta, & (j = 1,\cdots,6) \\ \sum_{e=1}^{N_E} \int_{-1}^{1} \int_{-1}^{1} G(x,x_0) \frac{\partial \phi_0(x)}{\partial n} |J_e(\xi,\eta)| d\xi d\eta, & (j = 7) \end{cases} \end{aligned} \tag{22}$$

where $J_e(\xi,\eta)$ is the Jacobian matrix relating the global coordinates and the local intrinsic coordinates in the e-th element.

For the traditional boundary element method, after assembling the equations for each element, Eq. (22) can be equivalent to computing the following set of linear equations:

$$[A]_{N\times N} \{\phi\}_N = \{B\}_N \tag{23}$$

where N is the number of unknowns. For the higher-order boundary element method, it is the total number of nodes on the body surface. $[A]$ is a dense matrix. It requires $O(N^3)$ operations and $O(N^2)$ memory allocation to solve this equation by direct method (such as Gaussian elimination). If the discretization of Eq. (23) is sufficiently well conditioned, iterative methods such as GCR can be used to reduce the problem computing cost from $O(N^3)$ to $O(N^2)$. In fact, switching from the direct method to an iterative method has an added benefit that makes further acceleration possible. The iterative method replaces the detailed manipulation of matrix elements with matrix–vector products in the direct method. This implies that the matrix is not explicitly required if the iterative method is used. Therefore, the double-layer integration and the single-layer integration in Eq. (14) are both equivalent to computing the matrix–vector product, together:

$$d = DU \tag{24}$$

As D is a dense matrix, it still requires $O(N^2)$ operations for forming DU. However, it could be systematically approximated in nearly N operations by separating D into two parts, i.e. D_{near} and D_{far}. D_{near}, associated with the nearby element-node contribution, is represented explicitly. Note that D_{near} is sparse, having nonzero entries only by $O(N)$. The contribution from the far elements, $d_{\mathrm{far}} = (D - D_{\mathrm{near}})U$, is approximated for rapid computation. In the pFFT method, d_{far} is approximated by representing far elements

with point singularities residing on a uniform grid. The fact that all the point singularities are on a uniform grid makes it possible to rapidly calculate potentials owing to those point singularities using the Fast Fourier Transform (FFT). Fig. 2 is a schematic diagram of the steps in the algorithm of the pFFT method. Instead of computing all interactions directly, one must follow a series of steps including grid set-up, projection, computing grid potentials, interpolation and direct interaction and precorrection:

(1) Grid set-up:
Consider the right-parallelepiped overlaying the problem geometry after it has been discretized by isoparametric elements. The right-parallelepiped can be subdivided into $M_x \times M_y \times M_z$ array of small cubes formed by the grid so that each small cube contains only a few elements. We refer to these small cubes as cells. In each cell, grid singularities are set in the direction of x, y and z. Empirical results indicate that a $3 \times 3 \times 3$ array of grid singularities per unit cell will approximate the potential well enough to ensure that the solution to Eq. (24) is accurate to 0.1% [25]. And then the number of total grid singularities N_g can be obtained. Apparently, N_g is coarser than N, as shown in Fig. 3. The grid singularities extends outside the problem domain in Fig. 3(b) because the number of grid points is required to be a factor of two for FFT operations.
The relationship of cells, elements and nodes should be established in this step. For the higher-order boundary element method, whether both the element and the node belonging to the same cell need to judge, because the projection step is based on the integral over elements, and the interpolation step need to calculate the potential on the nodes. In this statement, an element belongs to a cell if the centroid of the element is in this cell. The nearby elements of a given element are those elements in the 27 cells that share a vertex with the given element's cell. They will be used at the "Direct interaction and precorrection" step.

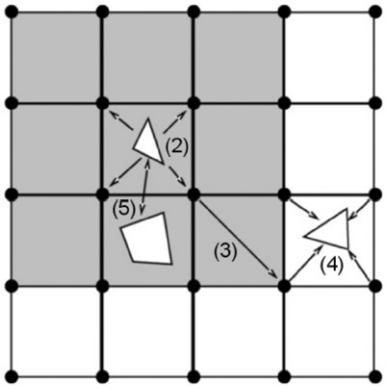

Fig. 2. Two-dimensional representation of the precorrected-FFT (pFFT) algorithm.

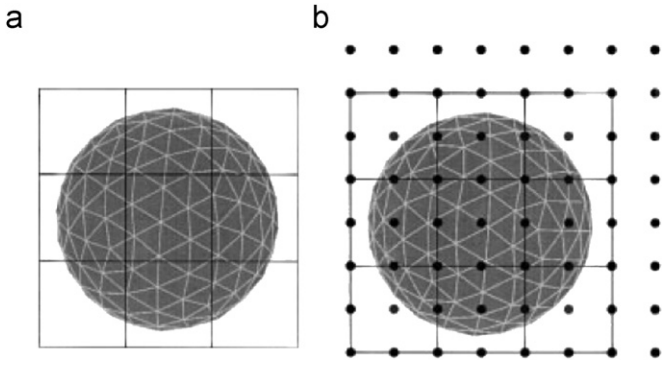

Fig. 3. Sketch of the right-parallelepiped and grid singularities (a) Right-parallelepiped. (b) Grid singularities.

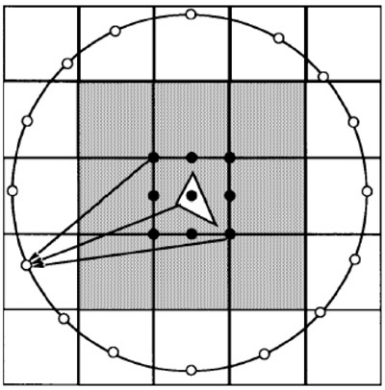

Fig. 4. Two-dimensional pictorial representation of the grid projection scheme.

(2) Projection:
Numerically evaluate the projection operator that can replace the singularity distributions on the body elements with an equivalent set of grid singularities. These are matrices deduced from a collocation problem for each cell that matches, at a set of test points, the potential due to the grid singularities with the potential due to the singularity distributions on the elements (Fig. 4). Since the projection is made once for each element, this step requires $O(N)$ computational time. The essential idea in this step is that the operator is based on the fundamental solution of the Laplace equation, not on the particular Green function for the problem. For wave sources distribution, the grid singularities' strength q_i can be sought in:

$$\sum_{i=1}^{I} q_i \frac{1}{\|r_j - r_i\|} = \sum_{k=1}^{K_m} \sigma_k \int_k \frac{1}{\|r_j - r_k\|} dr_k \quad j = 1,J \tag{25}$$

where I grid points, J projection test points and K_m elements are in the cell with the source distributions σ_k. The similar expression for replacing dipole distributions with grid singularities is

$$\sum_{i=1}^{I} q_i \frac{1}{\|r_j - r_i\|} = \sum_{k=1}^{K_m} \sigma_k \int_k \frac{\partial}{\partial n_\xi} \left(\frac{1}{\|r_j - r_k\|} \right) dr_k \quad j = 1,J \tag{26}$$

The precision of the above method is mainly dependent on the situation of the test points. A good choice are Gaussian quadrature points on a surrounding sphere, whose radius is twice that of the diameter of the cell [26].

(3) Computing grid potentials
This step is to find the potential on the grid points owing to these grid singularities on the same set of grids. This evaluation of the node-to-node interactions on a grid structure with uniform spacing is a three-dimensional discrete convolution. The influences between the grids points on the same cell, including the self-influence, are not relevant, and arbitrary values may be assigned to them. The influence of the grid singularities is decomposed into two components, one from $G_T(x-x_0, y-y_0, z-z_0)$, and the other from $G_H(x-x_0, y-y_0, z-z_0)$ in Eq. (13). On a uniform grid, G_T leads to a triply nested Toepliz matrix, G_H to a doubly nested Toepliz matrix in x and y and a Hankel matrix in z. From these matrices, it is straightforward to construct two circulant matrices with periodic elements as shown in [27]. Finally, the products of the circulant matrices and grid singularities' strength q_i can be evaluated efficiently from the relation $Cq_i = F^{-1}[F(C_1)F(q_i)]$ where C_1 denotes the first row of the circulant matrices, and F and F^{-1} denote the discrete

Fourier transform and the inverse Fourier transform, respectively [28]. The computational effort for the convolution is $O(N_g \log N_g)$, and the memory allocation is $O(N_g)$.

(4) Interpolation:
The interpolation step is to calculate the potential at each node on the body owing to the potentials at a set of grid points. This operator is the transpose of the complementary projection operator for point sources (nodes), not element distributions, as we are using a collocation method. That is, we use the transpose of the operator implied by

$$\sum_{i=1}^{I} \phi_i \frac{1}{\|r_j - r_i\|} = \sum_{k=1}^{K_n} \phi_k \frac{1}{\|r_j - r_k\|} \quad j = 1, J \tag{27}$$

where K_n is the total number of nodes in the cell. Again, it is important to note that only the fundamental solution of the Laplace equation appears in the definition of these operators [19]. In addition, interpolation Eq. (27) is adapted for both source and dipole distribution.

(5) Direct interaction and precorrection:
The previous four steps complete the matrix–vector multiplication in Eq. (24) by an indirect manner. The final step is to correct the influence of the parts of nearby elements for which the above 'interpolation–projection' method is not valid. Use the projection operators, the Green function, and the interpolation operators to pre-compute and subtract from these nearby elements' influences. And then, directly compute the nearby elements' influences for each element using the conventional calculations.
In this paper a GCR iterative method is employed. The right-hand side of Eq. (14) is computed first, and the result is regarded as an iterative initial value of the left matrix–vector operation. The efficiency of the pFFT method could be further improved through exploiting the frequency-independence of many of the algorithm's steps. Only the "Direct Interaction and Precorrection" and "Computing Grid Potentials" steps are frequency dependent. This means that the frequency independent set-up steps of the algorithm may be performed once and re-used at each frequency in a sweep of frequencies for radiation and diffraction analysis.

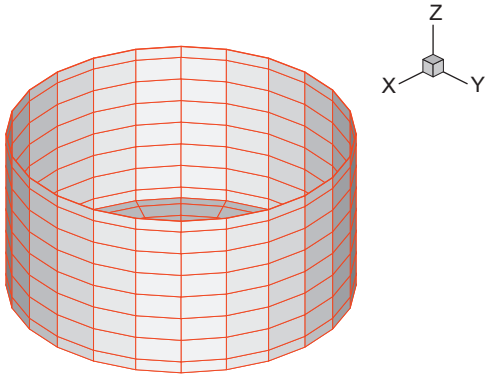

Fig. 5. Sketch of the mesh on the truncated vertical circular cylinder.

4. Validation and discussion

In this paper, all numerical codes have been implemented in Visual FORTRAN 6.5, and the computations have been tested on a computer with a 2.01 GHz processor and 2 GB of RAM. The calculation is carried out in the double precision. For the resulting matrix equation, the GCR is used, and the iteration is stopped when the module of the relative residual is smaller than 10^{-5}.

4.1. Truncated cylinder

As an example, a truncated vertical circular cylinder of radius $r=1.0$ and draft $T=1.0$ in deep water is considered. The rotation center is defined at the point (0, 0, 0). A mesh scheme of $8\times24+24\times8$ (circular, 24; vertical, 8; radius at the bottom, 8) for the truncated cylinder is shown in Fig. 5. The comparisons of exciting forces and hydrodynamic coefficients between the present method and a traditional HOBEM [7] are given in Figs. 6–8. The non-dimensional wave number range $ka=0.1$–2.0 and $\Delta ka=0.1$ are considered in the present study. From the figures, it can be seen that good agreements are obtained between the traditional HOBEM and the present method.

To further validate the present method, the comparison of wave elevation around the truncated cylinder, at points $(-1.1, 0)$, (0.0, 1.1) and (1.1, 0.0), with the traditional HOBEM is also shown in Fig. 9. Apparently, the results of present method agrees well with the traditional HOBEM. From all these comparisons, the accuracy of the present method is validated.

For illustrating the advantages of the present method in computing cost and computer memory, the above truncated cylinder at the non-dimensional wave number $ka=1.0$ is taken as an example. Four different methods are chosen for different discretization, and the corresponding results are shown in Fig. 10. The abbreviation N stands for the number of unknowns. "HOBEM-Direct" and "HOBEM-Iterative" indicate the traditional HOBEM with direct and iterative solvers, respectively. "HOBEM-pFFT A" and "HOBEM-pFFT B" indicate the HOBEM accelerated by pFFT overlaying the problem geometry with $7\times7\times7$ and $15\times15\times15$ cells, respectively. These cell-overlay schemes could make the number of grid points close to a factor of 2 for advanced efficiency.

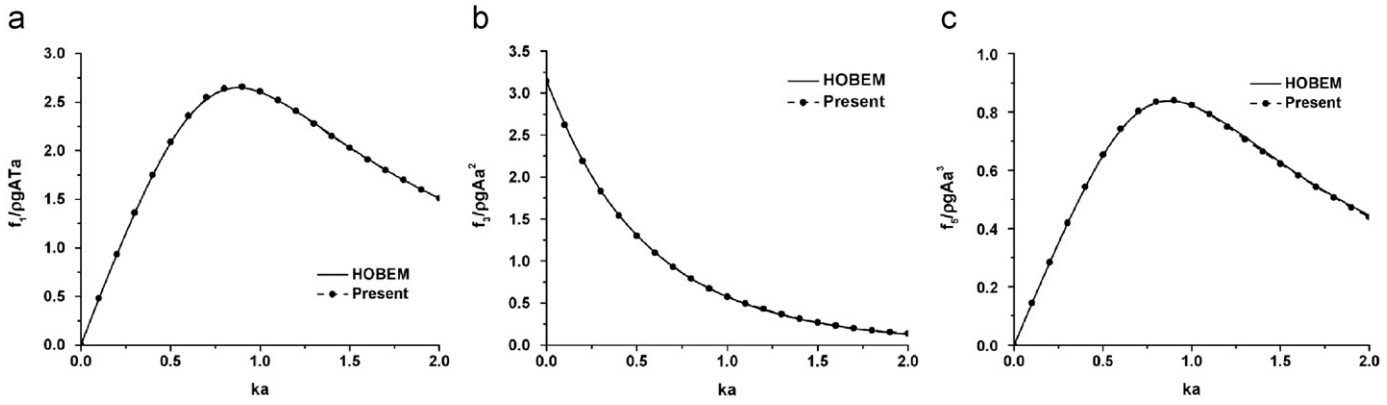

Fig. 6. Exciting force on the truncated vertical circular cylinder. (a) Surge. (b) Heave. (c) Pitch.

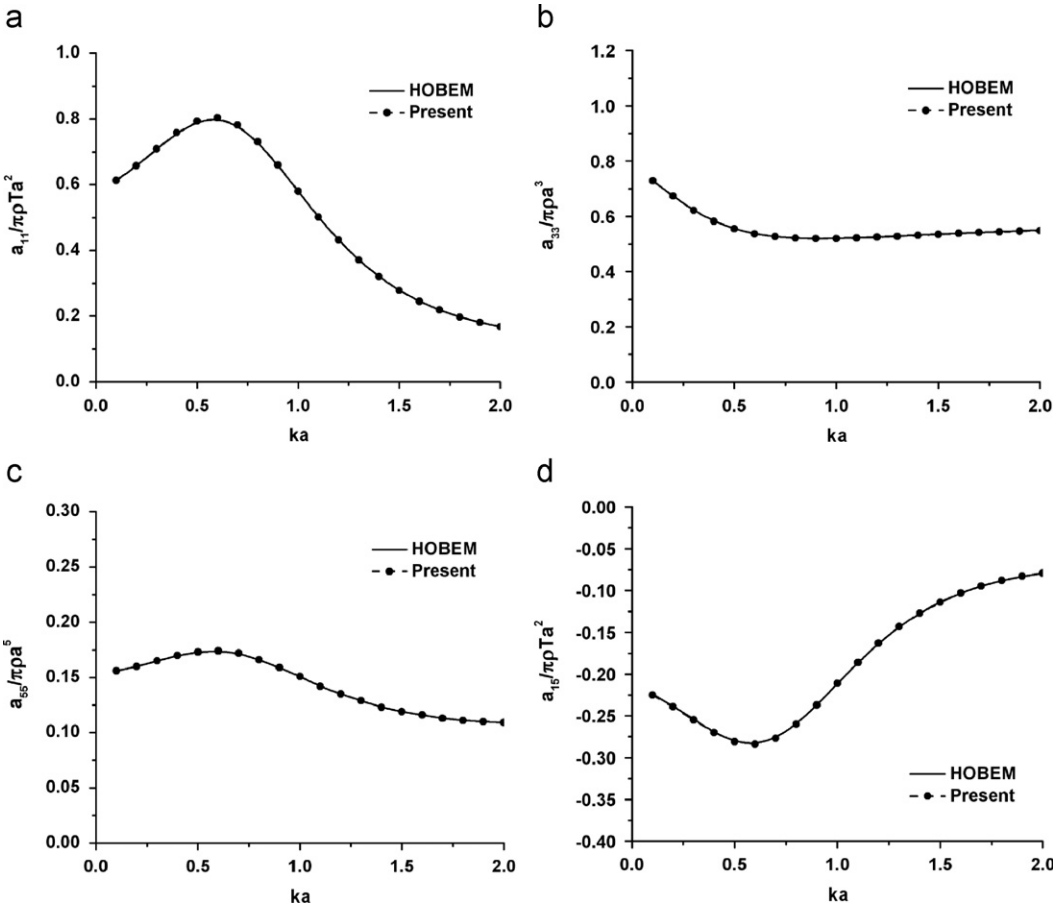

Fig. 7. Added mass of the truncated vertical circular cylinder. (a) Surge, (b) Heave. (c) Pitch. (d) Cross-coupling surge and pitch.

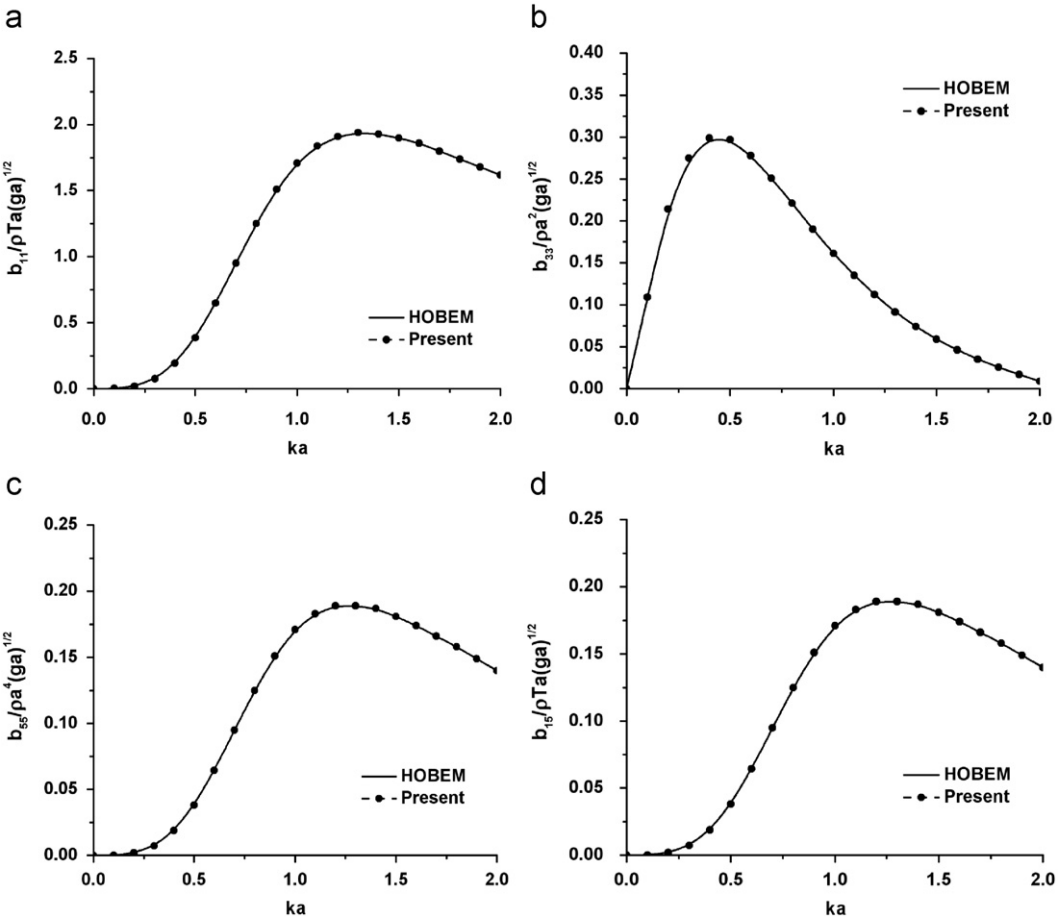

Fig. 8. Radiation damping of the truncated vertical circular cylinder, (a) Surge. (b) Heave. (c) Pitch. (d) Cross-coupling surge and pitch.

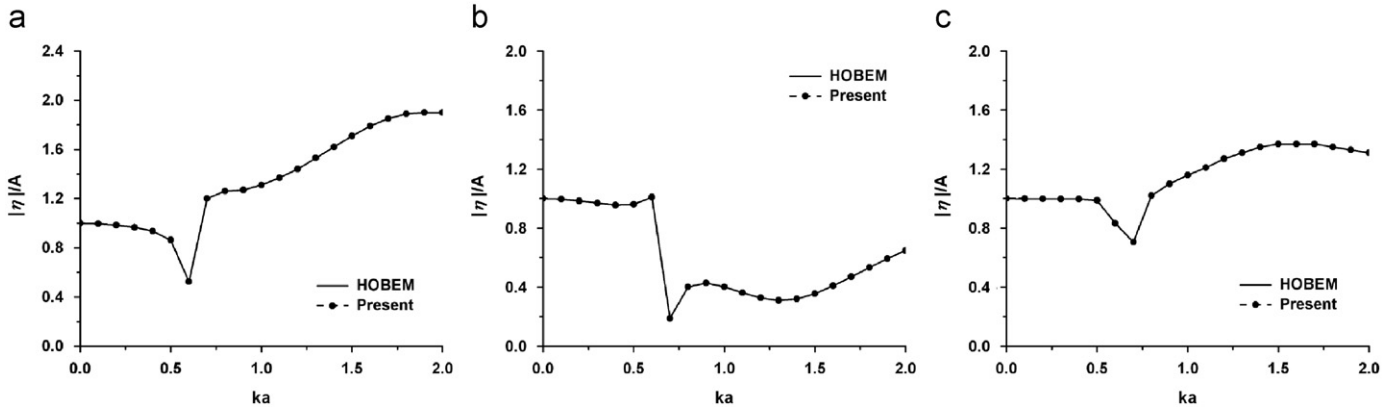

Fig. 9. Wave elevation near truncated vertical circular cylinder. (a) (− 1.1, 0.0). (b) (1.1, 0.0). (c) (0.0, 1.1).

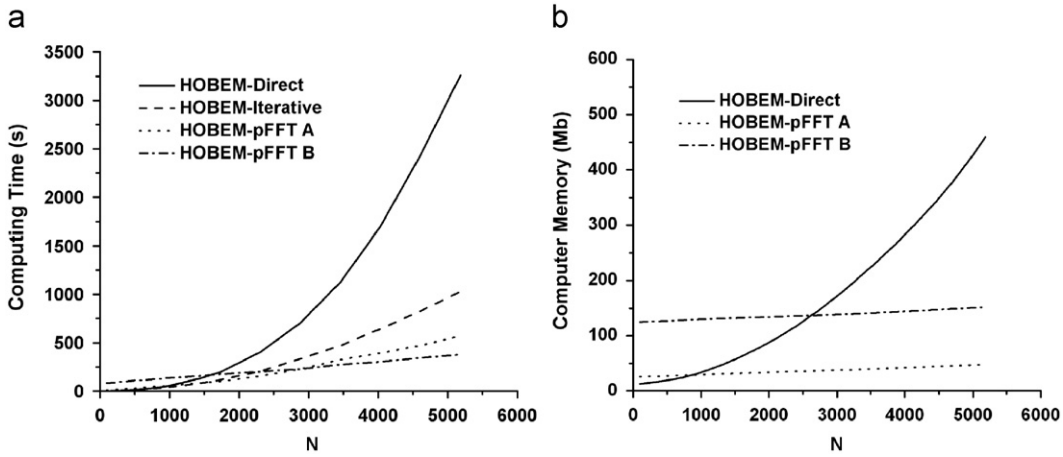

Fig. 10. Comparison of the computing cost and computer memory (a) Computing time. (b) Computer memory.

As for computing cost, "HOBEM-Iterative" is faster than "HOBEM-Direct." If the number of unknowns is larger than 1000 and 1700, HOBEM-pFFT A and HOBEM-pFFT B are faster than traditional HOBEM, respectively. If the number of unknowns is larger than 2800, HOBEM-pFFT B has a lower computing cost than HOBEM-pFFT A. This means that the greater number of cells in the pFFT method should be chosen to reduce the computing cost if the unknowns are large. As for computer memory, the pFFT methods increase linearly with the increase of the unknowns. If the number of unknowns is larger than 1000 and 2600, the HOBEM-pFFT A and HOBEM-pFFT B need less storage than the traditional HOBEM, respectively. Another observation is that the computer storage of the HOBEM-pFFT B is always larger than that of the HOBEM-pFFT A, and that the additional memory is nearly constant for different numbers of unknowns. This is the reason that the major difference between these two systems is in the computing FFT and the inverse-FFT. These steps are independent of the number of unknowns. The HOBEM-pFFT A needs $32\times32\times32$ units of memory in point singularities (wave sources or dipoles), but the HOBEM-pFFT B needs $64\times64\times64$ units of memory. This means that the computer memory would be increased in the present method if more cells are chosen. Actually, even if the HOBEM-pFFT B with 5000 unknowns is chosen, the computer memory is still less than 200MB. It is apparent that computer memory cannot become the major factor that limits the use of the present method in an ordinary computer. Therefore, the optimization method for minimizing the computing cost is suggested.

In the process of the present method the comparisons of computing cost in different parts are given in Table 1. A and B stand for HOBEM-pFFT A and HOBEM-pFFT B schemes, respectively. From this table, we can see that the cost of Project and Interpolation steps are always small. The major parts of the computing cost are at the Grid Potentials and Precorrected steps. The Grid Potentials step considers the same computing cost in different unknowns. They are about 4.6s and 63s for HOBEM-pFFT A and HOBEM-pFFT B, respectively. Actually, this is only the node-to-node interactions between point singularities on the grid structure at the Grid Potentials step. For the HOBEM-pFFT A, it is a three-dimensional discrete convolution by the FFT and inverse-FFT methods for 32 points per dimension. However, it becomes 64 points per dimension when the HOBEM-pFFT B is used. If the number of unknowns is small, the computing cost at the Precorrected step is small, depending on the number of unknowns. The major computing cost is at the Grid Potentials step, which leads to a lower efficiency than the traditional HOBEM, especially for HOBEM-pFFT B. With the increase of unknowns, the major part of the computing cost is at the Precorrected step. In this case it can be understood that the whole problem domain is divided into N_c sub-domains, where N_c is the number of cells. So the computing cost is reduced from $O(N^2)$ by the traditional HOBEM with iterative solver to $N_c\times O(N_s^2)$, $N_s=N/N_c$ by the present method. This is also the reason that the HOBEM-pFFT B scheme ($N_c=15$) is faster than the HOBEM-pFFT A scheme ($N_c=7$) by reason of a large number of unknowns.

4.2. Four-cylinder structure

To further state the superiority of present method, another computation is carried out for a fixed four-cylinder structure with radius $r=a$ and draft $T=3a$ in deep water (Fig. 11). The centers of

Table 1
Comparison of the CPU cost (s) in different parts of pFFT methods.

N	Project		Grid Potentials		Interpolation		Precorrected		Others		Total	
	A	B	A	B	A	B	A	B	A	B	A	B
97	0.17	0.25	4.81	60.00	0.38	3.59	4.28	21.48	0.00	0.02	9.64	85.34
217	0.36	0.48	4.55	62.75	0.41	3.63	9.21	23.58	0.01	0.03	14.53	90.47
385	0.61	0.80	4.53	63.59	0.44	3.64	18.31	33.19	0.02	0.03	23.91	101.25
481	0.69	0.95	4.63	64.03	0.42	3.63	23.31	41.27	0.02	0.02	29.06	109.89
721	0.98	1.31	4.61	64.06	0.45	3.69	37.84	49.67	0.02	0.05	43.91	118.78
961	1.36	1.73	4.59	62.84	0.47	3.69	46.55	67.17	0.03	0.06	53.00	135.50
1441	1.97	2.91	4.50	63.33	0.50	3.77	78.87	86.81	0.06	0.06	85.91	156.88
1729	2.33	3.41	4.61	62.24	0.55	3.79	93.70	106.73	0.06	0.07	101.25	176.23
2305	3.08	3.73	4.58	62.92	0.58	3.81	147.28	131.64	0.05	0.08	155.56	202.19
2881	3.84	4.42	4.63	67.61	0.64	3.91	220.31	152.45	0.08	0.11	229.50	228.50
3457	4.59	5.14	4.64	63.73	0.72	4.00	314.55	202.52	0.11	0.09	324.61	275.48
4033	5.31	6.06	4.67	68.09	0.69	4.05	382.73	225.63	0.13	0.11	393.53	303.94
4609	10.53	10.84	4.63	64.08	0.78	4.02	457.03	266.42	0.11	0.14	473.08	345.50
5185	6.81	7.83	4.66	63.42	0.84	4.06	558.33	302.00	0.14	0.11	570.78	377.42

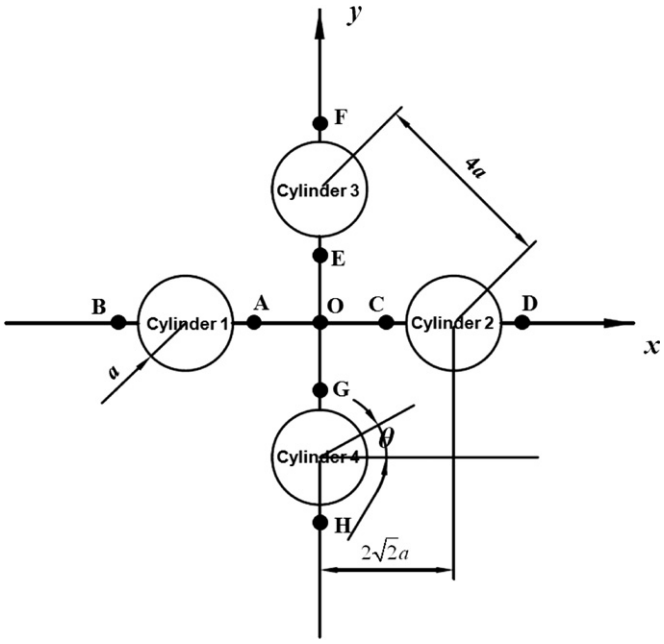

Fig.11. Four-cylinder structure in regular wave.

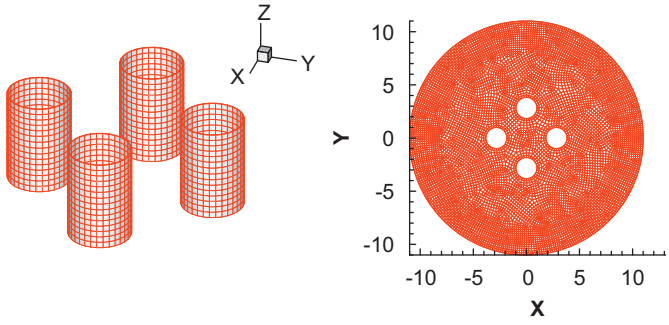

Fig. 12. Sketch of the meshes on the body surface and free surface on four-cylinder problem.

four cylinders locate in $(\pm 2.828a,\ 0)$ and $(0, \pm 2.828a)$, respectively. Waves are from the direction along the angle of $\theta=45^\circ$, and the wave amplitude is A. The quadrilateral unstructured meshes of the size $0.2a$ are employed on the wetted body surface and the free surface, as shown in Fig. 12. Based on the conclusion of Evans and Porter [29], the near-trapping resonance would occur for $ka=1.66$. In this study, the non-dimensional wave number $ka=1.66$ is considered, along with the non-dimensional wave number range $ka=0.1$–2.0 and $\Delta ka=0.1$ are considered.

Table 2
Coordinates of test points near four-cylinder structure.

Cylinder	Situation	Serial number	Coordinates
Cylinder 1	Inside the structure	A	$(-1.728a, 0)$
	Outside the structure	B	$(-3.928a, 0)$
Cylinder 2	Inside the structure	C	$(1.728a, 0)$
	Outside the structure	D	$(0, 3.928a)$
Cylinder 3	Inside the structure	E	$(0, 1.728a)$
	Outside the structure	F	$(0, 3.928a)$
Cylinder 4	Inside the structure	G	$(0, -1.728a)$
	Outside the structure	H	$(0, -3.928a)$

For validation of the present method, wave elevation distribution of eight points are selected here. The locations of these points are tabulated in Table 2 and the comparison with the tradional HOBEM is shown in Fig. 13. Apparently, the present results are in good agreement with those of the traditional HOBEM. In here, a distinctive feature is an apparent peak that occur near $ka=1.66$ at the inside points (A, C, E, G) of the structure. At the same time, a negative peak occur at points D, F and G. In addition, the wave elevation of point B is smaller than that of point A, though it is a peak near $ka=1.66$. That means the wave energy inside of the four-cylinder structure is larger than that of outside when near-trapping phenomenon happen.

The magnitudes of the horizontal and vertical wave forces on different cylinder are shown in Figs. 14 and 15. The present method and the traditional HOBEM are in good agreement. From Fig. 14, we can be seen that a magnitude of the peak appears on each cylinder near $ka=1.66$. It is an obvious relationship between horizontal exciting force and wave elevation around the cylinder, especially the water level difference and phase between inside and outside of the structure.

The non-dimensional wave elevation distributions around four-cylinder structure are shown in Fig. 16. When $ka=1.00$, the wave elevation is a little larger at the back of structure for long period wave. The wave reflection is stronger when $ka=2.00$, so that the wave elevation at downstream of the structure become smaller. For the case of $ka=1.66$, wave energy is focused inside of the structure, which leading to the inside wave elevation large. Whereas, the outside wave elevation is quite small, especially at

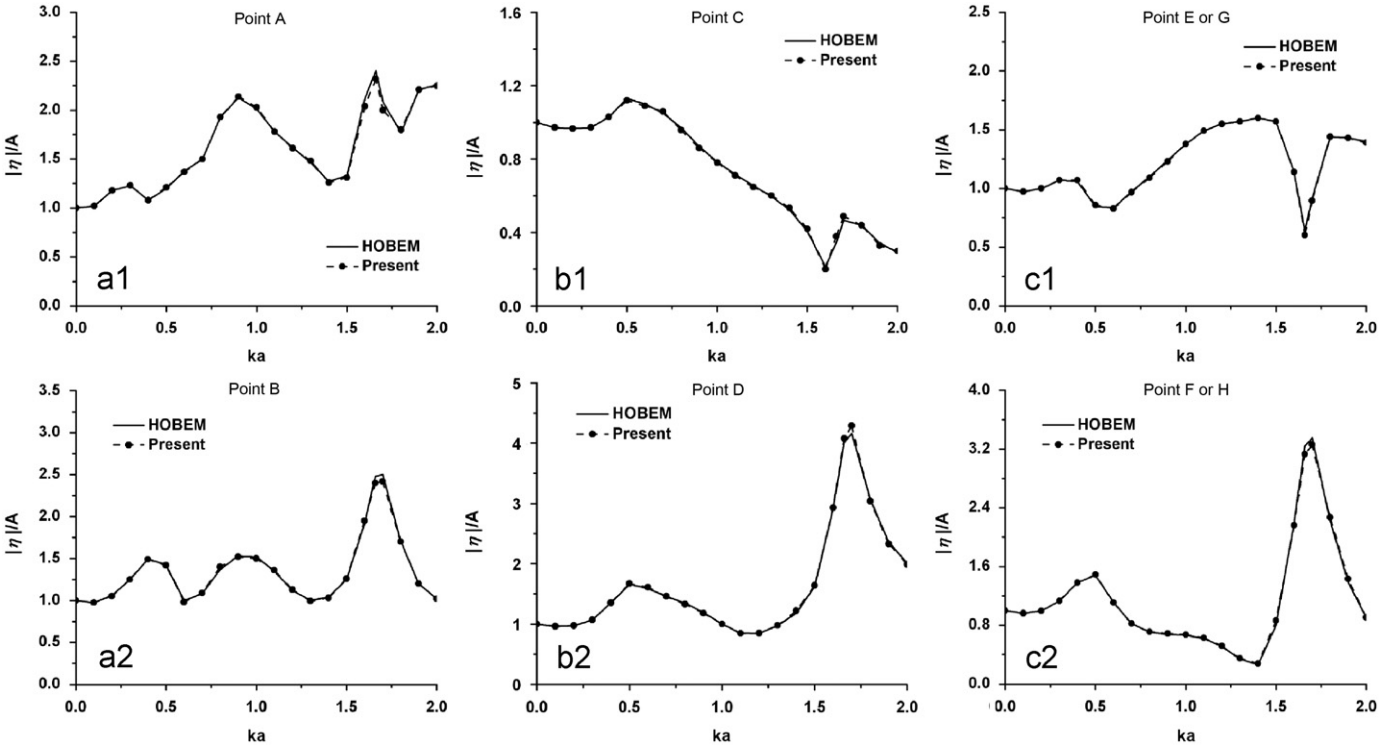

Fig. 13. Variation of wave elevation at typical points with *ka*. (a1) Point A. (b1) Point C. (c1) Point E or G. (a2) Point B. (b2) Point D. (c2) Point F or H.

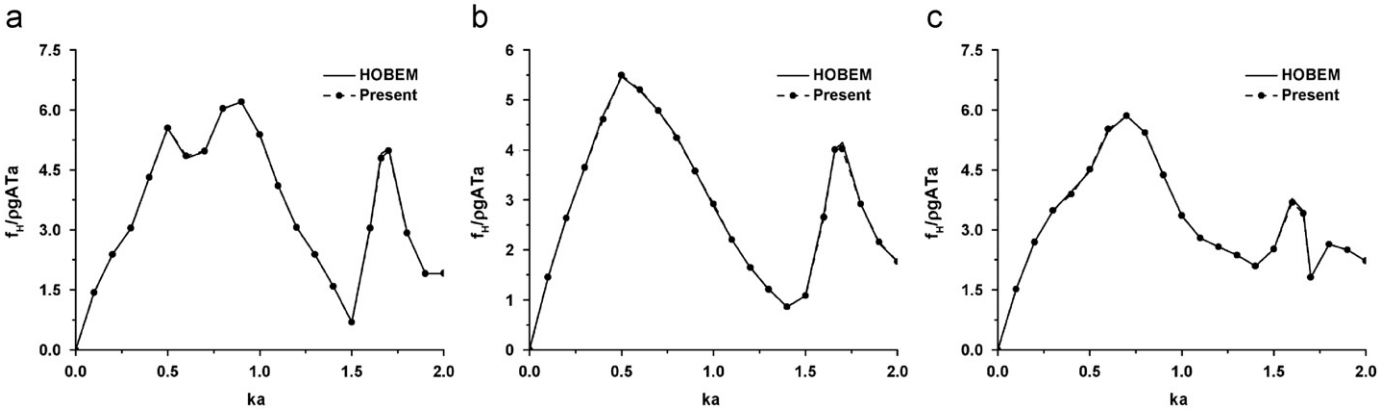

Fig. 14. Horizontal wave force on cylinder. (a) Cylinder 1, (b) Cylinder 2, (c) Cylinder 3 or 4.

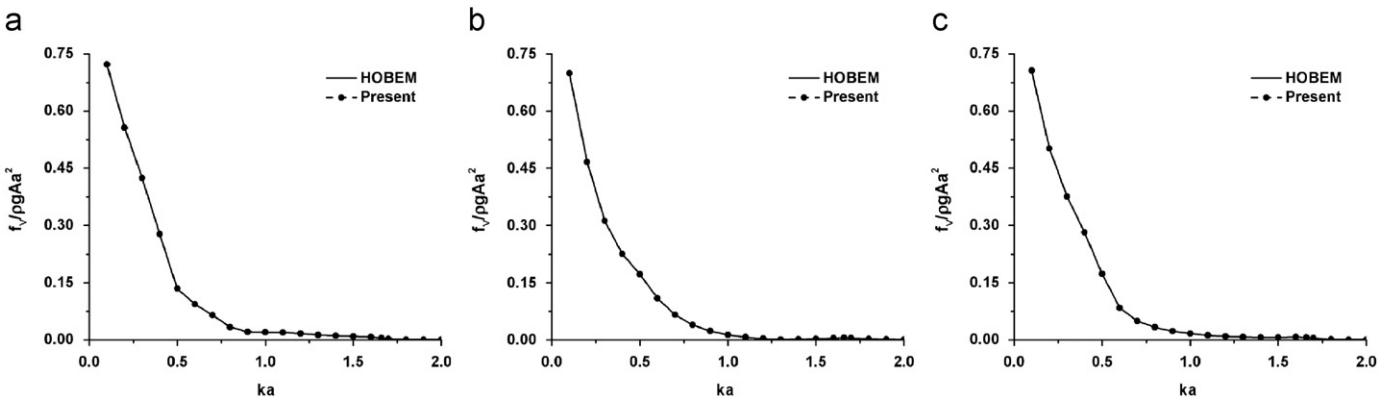

Fig. 15. Vertical wave force on cylinder. (a) Cylinder 1, (b) cylinder 2, (c) cylinder 3 or 4.

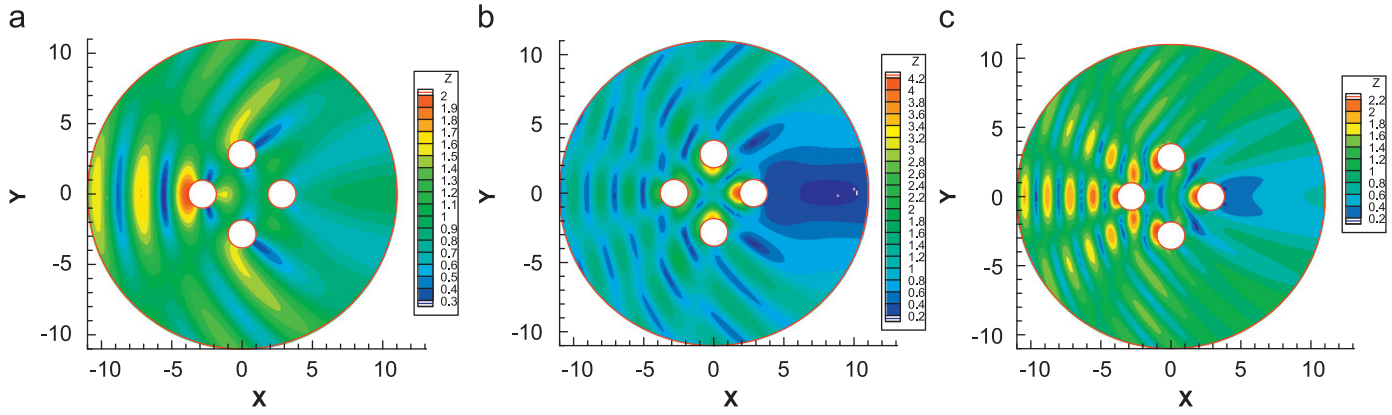

Fig. 16. Wave distribution around four-cylinder structure. (a) $ka=1.00$, (b) $ka=1.66$, (c) $ka=2.00$.

Table 3
Convergent examinations of meshes for exciting forces on the entire structure.

N	Surge exciting forces (10^3 kN)				Heave exciting forces (10^3 kN)				Pitch exciting forces (10^3 kN)			
	$T=5$ s	$T=10$ s	$T=15$ s	$T=20$ s	$T=5$ s	$T=10$ s	$T=15$ s	$T=20$ s	$T=5$ s	$T=10$ s	$T=15$ s	$T=20$ s
1272	0.52	8.10	5.42	8.34	0.09	3.28	6.20	23.11	16.43	486.53	1957.30	4628.30
3208	3.09	6.13	6.08	7.92	0.06	2.04	7.10	21.33	19.93	564.78	1704.00	4779.30
4880	3.46	5.52	6.29	7.73	0.05	1.71	7.31	21.12	20.42	596.94	1662.70	4817.10
12240	3.46	5.52	6.30	7.73	0.05	1.70	7.30	21.11	20.37	595.87	1660.90	4814.50

the downstream of the structure. One would perhaps more sheltering and that $|\eta/A|<1$. This behavior is similar as the Neumann resonance mode by Walker and Eatock Taylor [30].

4.3. Double array truncated cylinders

To validate the present method in a more complex application, a double array of 2×8 truncated cylinders in head seas of a unit wave amplitude with different periods is considered. Such a type of configuration can be proposed for floating bridges, floating airports and mobile offshore bases etc. The radius and draft of each truncated cylinder might be defined as 12 m and 20 m, respectively. The distance between the axes of adjacent cylinders is $2d=64$ m. Apparently there is a clear interference that could not be predicted accurately by analyzing only a single cylinder. Convergent examinations of meshes are performed for surge, heave and pitch exciting forces on the entire structure. The whole structure is discretized with 1272, 3208, 4880 and 12240 nodes. As shown in Table 3, the surge, heave and pitch exciting forces are calculated under different mesh schemes for the periods $T=5$ s, 10 s, 15 s and 20 s. It is apparent that the 4880-node scheme should be chosen, and the sketch of this mesh scheme is shown in Fig. 17. In this figure the z-axis of the coordinate system is doubly enlarged for a clearer display.

Numerical results of the 4880-node scheme are shown in Fig. 18. Based on the analysis in section 4.1, the HOBEM-pFFT B scheme is chosen for a lower computing cost. The incident wave periods range from 5 s to 20 s. The time interval Δt is chosen as 0.1 s for 5–10 s, and 1.0 s for 10 s–20 s. For heave force, the present method could obtain enough precision for all the periods. For the surge force and pitch moment, it can be seen that the present method could obtain accurate results for most periods, although it does not capture the extreme large surge force near $T=6.0$ s owing to the influence of near-trapping mode resonance, which causes the tendency of the linear system to be ill-conditioned [31]. This leads to a large error if the iterative solver is employed.

To further illustrate the computing efficiency of the present method, Table 4 gives the computing costs for different wave periods. The "symmetry" in this table indicates that the two planes of symmetry are exploited in the traditional HOBEM with either direct or iterative solvers. "Acc%" is the ratios of the other methods to the traditional HOBEM marked by "Direct." Apparently the present method is the fastest one in these five schemes. Moreover, the symmetry optimizations must be canceled if structures have no symmetry planes. In addition, the size of the structure is usually larger than that in this example, such that a mobile offshore base is generally made up of 50 cylinders [32]. Therefore, the present method can produce a higher efficiency in engineering. Finally, for different wave periods, the computing cost of the present method is nearly the same, which is quite different from the FMM [33].

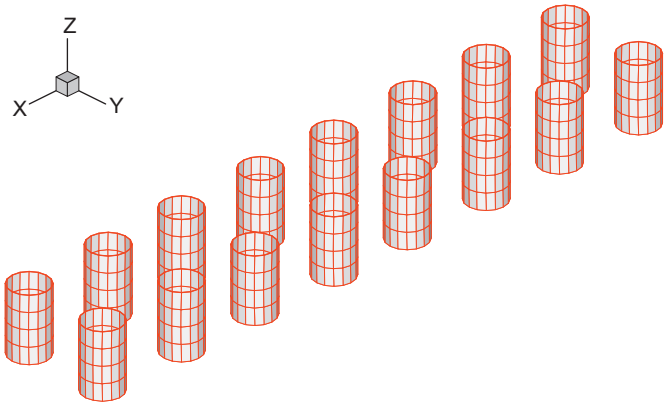

Fig. 17. Sketch of the mesh on the double array of 2×8 cylinders.

5. Conclusions

In this paper, the pFFT higher-order boundary element method is successfully applied to reduce the computational cost and memory

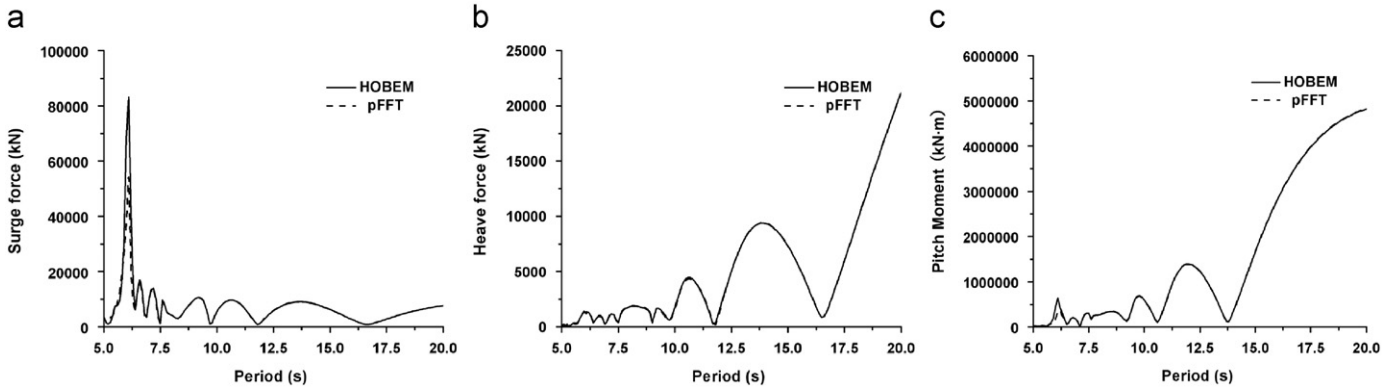

Fig. 18. Exciting forces on the entire double array of 2×8 truncated cylinders in head seas of 1m wave amplitude at different periods. (a) Surge force. (b) Heave force. (c) Pitch moment.

Table 4
Comparison of CPU cost(s) using different methods for the double array of 2×8 truncated cylinders.

Period	Direct	Iterative	Direct-symmetry	Iterative-symmetry	pFFT method
5	2724.64	900.55	503.75	428.23	305.61
6	2759.81	922.06	503.89	432.16	301.63
7	2762.16	915.58	502.34	424.50	300.61
8	2749.09	896.64	498.16	412.09	302.72
9	2742.94	896.11	501.48	414.64	305.05
10	2740.27	895.98	500.28	415.84	309.13
11	2747.63	906.72	494.89	422.91	306.16
12	2707.02	874.62	495.17	411.11	305.55
13	2727.02	884.01	494.53	410.50	305.34
14	2759.06	897.16	493.86	407.63	305.28
15	2745.03	892.75	493.67	410.23	304.59
16	2745.47	895.86	496.52	413.13	304.17
17	2740.06	890.08	496.08	410.05	304.41
18	2716.11	877.79	495.59	409.73	305.06
19	2686.80	864.80	495.25	411.41	304.98
20	2686.23	864.09	494.63	410.97	307.31
Average time	2732.49	889.44	496.60	413.20	305.03
Acc.%	100.00%	32.55%	18.17%	15.12%	11.16%

by $O(N \log N)$ and $O(N)$ in analyzing the hydrodynamic problems, respectively. By using an infinite deep free-surface Green function, the present method can be easily extended to infinite deep water, which is superior to the Fast Multipole method (FMM). According to the numerical experiment, the optimal variable of pFFT mesh is recommended to minimize time lost. The computational results show that the present method is more efficient than the traditional boundary element method for large-scale problems. In the present method, the major computing cost is at the step of "direct interaction and precorrection" if the number of unknowns is large. The solution of the linear system varies by the present method and is independent as to the period of the incident waves. In the end, a four-cylinders structure and a double array of 2×8 truncated cylinders is calculated. The results show that the present method could obtain a high precision for the multi-bodies problem. This method is faster than the traditional HOBEM, even if two planes of symmetry are exploited in the latter. Therefore, the proposed technology is feasible for solving large-scale wave–body problems.

Acknowledgments

The present work is supported by the National Natural Science Foundations of China (Grant nos. 11072052 and 50921001), the Important National Science & Technology Specific Projects of China (Grant no. 2008ZX05026-02) and the Open Fund of Key Laboratory of Renewable Energy and Gas Hydrate of Chinese Academy of Sciences (Grant no. Y007ka).

References

[1] Hess JL, Smith AMO. Calculation of non-lifting potential flow about arbitrary three-dimensional bodies. J Ship Res 1964;8:22–44.
[2] Garrison CJ. Hydrodynamic loading on large offshore structures: three-dimensional source distribution method. Numer Methods Offshore Eng 1978.
[3] Korsmeyer FT, Lee CH, Newman JN, Sclavounous PD. The analysis of wave effects on a tension-leg platform. In: Proceedings of the offshore mechanical and arctic engineering, vol. 2; 1988. p. 1–15.
[4] Liu YH, Kim CH, Lu XS. Comparison of higher-order boundary element and constant panel methods for hydrodynamic loadings. J Offshore Polar Eng 1991;1(1):8–17.
[5] Eatock Taylor R, Chau FP. Wave diffraction—some developments in linear and non-linear theory. Offshore Mech Arctic Eng 1992;114:185–94.
[6] Eatock Taylor R, Teng B. The effect of corners on diffraction/radiation forces and wave drift damping. In: Proceedings of the offshore technology conference, OTC7187, Houston ;1993. p. 571–81.
[7] Teng B, Eatock Taylor R. New higher-order boundary element methods for wave diffraction/radiation. Appl Ocean Res 1995;17(2):71–7.
[8] Teng B, Saito M, Kato S. Mean drift force on a huge shallow drafted floating barge. In: Proceedings of the 13th ocean engineering symposium, Tokyo; 1995. p. 337–344.
[9] Maeda H, Masuda K, Miyajima S, Ikoma T. Hydroelastic responses of pontoon type very large floating offshore structure. J Soc Nav Archit. Jpn 1995;178: 203–12.
[10] Sun L, Taylor PH, Eatock Taylor R. First and second order wave effects in narrow gaps between moored vessels. In: Proceedings of marine operation specialty symposium, MOSS, Singapore; 6–7 March 2008. p. 113–124.
[11] Zheng YH, Shen YM, Xia J. Numerical solution of a mathematical model for water waves in large coastal areas. Atca Oceanol Sin 2000;19(4):17–23.
[12] Greengard L, Rokhlin V. A fast algorithm for particle simulations. J Comput Phys 1987;73:325–48.
[13] Utsunomiya T, Watanabe E, Nishimura N. Fast multipole algorithm for wave diffraction/radition problems and its application to VLFS in variable water depth and topography. In: Proceedings of OMAE '01–5202.
[14] Utsunomiya T, Watanabe E. Wave response analysis of hybrid-type VLFS by accelerated BEM. Hydroelasticity in marine technology.2003 pp. 297–303.
[15] Teng B, Gou Y. Fast multipole expansion method and its application in BEM for wave diffraction and radiation. Proceedings of the international offshore and polar engineering conference, ISOPE 3; 2006. p. 318–325.
[16] Lee C-H, Newman JN. Computation of wave effects using the panel method. Numer Models Fluid-Struct Interact 2004.
[17] Phillips JR, White JK. A precorrected-FFT method for electrostatic analysis of complicated 3-D structures. IEEE Trans Comput-Aided Des 1997;16(10): 1059–72.
[18] Korsmeyer FT, Klemas TJ, White JK, Phillips JR, Fast hydrodynamic analysis of large offshore structures. In: Proceedings of ninth international offshore and polar engineering conference, ISOPE, Brest; 1999. p. 27–34.
[19] Kring D, Korsmeyer T, Singer J, White J. Analyzing mobile offshore bases using accelerated boundary element methods. Mar Struct 2000;13:301–13.
[20] Newman JN, Lee C-H. Boundary-element methods in offshore structure analysis. J Offshore Mech Arctic Eng 2002;124:81–9.
[21] John F. On the motion of floating bodies II. Commun Pure Appl Math 1950;3:45–101.
[22] Noblesse F. The Green function in the theory of radiation and diffraction of regular waves by a body. J Eng Math 1982;16:137–69.

[23] Newman J.N.. The approximation of free-surface Green functions. In: Wave asymptotics—Proceedings of the F. Ursell retirement meeting, Cambridge University Press; 1992. p. 107–135.
[24] Teng B, Gou Y, Ning DZ. A higher order BEM for Wave-current action with structure—directory computation of free-term coefficient and CPV integrals. China Ocean Eng 2006;20(3):395–410.
[25] Korsmeyer T, Phillips J, White JA. Precorrected-FFT algorithm for accelerating surface wave problems. Presented at the 11th workshop on water waves and floating bodies, Hamburg; 1996.
[26] Phillips J. Error and complexity analysis for a collocation-grid-projection plus Precorrected-FFT algorithm for solving potential integral equations with Laplace or Helmholtz kernels. In: Colorado conference on multigrid methods; April 1995.
[27] Loan CV. Computational frameworks for the fast Fourier transform. Philadelphia: SIAM; 1992.
[28] Strang G. Introduction to applied mathematics. Wellesley, Massachusetts: Wellesley-Cambridge Press; 1986.
[29] Evans DV, Porter R. Near trapping of waves by circular arrays of vertical cylinder arrays [J]. J Fluids Struct 1991;5:1–32.
[30] Walker DAG, Eatock Taylor R. Wave diffraction from linear arrays of cylinders [J]. Ocean Eng 2005;32:2053–78.
[31] Newman JN. Process in wave load computation on offshore structures, OMAE. Canada: Vancouver, B.C.; 2004.
[32] Lee C-H, Newman JN An assessment of hydroelasticity for very large hinged vessels. In: Proceedings 2nd international conference on hydroelasticity in marine technology, Kyushu, Japan; 1998. p. 27–36.
[33] Utsunomiya T, Watanabe E. Accelerated higher order boundary element method for wave diffraction/radiation problems and its applications. In: Proceedings 12th international offshore and polar engneering conference, Kyushu, Japan, vol. 3; 2002. p. 305–312.